

Clumpy filaments of the Chamaeleon I cloud: C¹⁸O mapping with the SEST*

L. K. Haikala^{1,2}, J. Harju², K. Mattila², and M. Toriseva²

¹ Swedish-ESO Submillimetre Telescope, European Southern Observatory, Casilla 19001, Santiago, Chile
e-mail: haikala@astro.helsinki.fi

² Observatory, PO Box 14, FI-00014 University of Helsinki, Finland

Received ; accepted

Abstract. The Chamaeleon I dark cloud (Cha I) has been mapped in C¹⁸O ($J = 1 - 0$) with an angular resolution of 1' using the SEST telescope. The large scale structures previously observed with lower spatial resolution in the cloud turn into a network of clumpy filaments. The automatic Clumpfind routine developed by Williams et al. 1994 is used to identify individual clumps in a consistent way. Altogether 71 clumps were found and the total mass of these clumps is 230 M_⊙. The dense 'cores' detected with the NANTEN telescope (Mizuno et al. 1999) and the very cold cores detected in the ISOPHOT serendipity survey (Tóth et al. 2000) form parts of these filaments but decompose into numerous 'clumps'. The filaments are preferentially oriented at right angles to the large-scale magnetic field in the region. We discuss the cloud structure, the physical characteristics of the clumps and the distribution of young stars. The observed clump mass spectrum is compared with the predictions of the turbulent fragmentation model of Padoan & Nordlund 2002. An agreement is found if fragmentation has been driven by very large-scale hypersonic turbulence, and if it has had time to dissipate into modestly supersonic turbulence in the interclump gas by the present time. According to numerical simulations, large-scale turbulence should have resulted in filamentary structures as seen in Cha I. The well-oriented magnetic field does not, however, support this picture, but suggest magnetically steered large-scale collapse. The origin of filaments and clumps in Cha I is thus controversial. A possible solution is that the characterization of the driving turbulence fails and in fact different processes have been effective on small and large scales in this cloud.

Key words. ISM:clouds – ISM:molecules – ISM:structure – individual objects: Chamaeleon I

1. Introduction

The dark cloud Cha I is one of the nearest low-mass star forming regions. The distance 150 pc to the cloud has been recently determined using the Hipparcos satellite data by Knude & Høg 1998. The elongated cloud with the apparent dimensions $\sim 0.5^\circ$ by $\sim 2^\circ$ is easily recognized on the ESO/SRC sky survey plates. A visual extinction map based on star counts on the ESO/SRC sky survey plates is presented in Toriseva & Mattila 1985 and a near-IR extinction map from DENIS *IJK* star counts by Cambrésy et al. 1997. Several signposts of past and present star formation are observed in the cloud. Three visually bright reflection nebulae (Ced 110, Ced 111 and Ced 112; Cederblad 1946) and an infrared reflection nebula (the IRN) are associated with Cha I.

More than hundred pre-main-sequence stars have been found in the cloud. Besides clusters around the visible reflection nebulae, these objects are scattered around its western mid part and the northern part. Evidence for ongoing star formation

near Ced 110 and Ced 112 is provided by observed molecular outflows (Mattila et al. 1989, Prusti et al. 1991) and two mm continuum sources (Reipurth et al. 1996). The research on Cha I until 1990 is reviewed by Schwartz 1991. A short summary of later large scale studies is given in the following.

A search for new young stellar objects in Cha I has been conducted by Cambrésy et al. 1998 using DENIS *IJK* photometric data. Most sources were distributed in a similar way to the known member candidates in the central and northern parts of the cloud. Only few young star candidates were found in the southern part. A deeper *JHK* study by Gómez & Kenyon 2001 confirmed these results. New candidate member stars have been found using *L*-band photometry (Kenyon & Gómez 2001) and *JHK* variability studies (Carpenter et al. 2002). Using ISOCAM observations Persi et al. 2000 found clusters of sources with mid-IR excess around the three reflection nebulae. A number of sources with mid-IR excess is seen also in the very eastern and western parts of the cloud but only one in the dense region southwest of Ced 111.

The multicolour IRAS images (Boulanger et al. 1990; Boulanger et al. 1998) outline the dense parts of Cha I. FIR

Send offprint requests to: L. Haikala

* Based on observations collected at the European Southern Observatory, La Silla, Chile

ISOPHOT observations of the southern part are reported in Haikala et al 1998. Besides the emission from the strong IR point sources in the reflection nebulae Ced 110 and 111 and the IRN, extended FIR emission is seen to coincide with the extinction features mapped by Toriseva & Mattila 1985 and Cambr esy et al. 1997. In particular two extended dust emission maxima are seen southwest of Ced 111. These dust emission maxima were detected also by the ISOPHOT 170 μm Serendipity Survey observations of Cha I (T oth et al. 2000). However, up to now no FIR point sources have been detected in these maxima.

Compared to the major star formation regions in the northern sky, radio molecular line observations of the Chamaeleon region have been few. The first large-scale radio molecular line mappings of the cloud were made with the Parkes 64-m telescope in the 6 and 18 cm transitions of H₂CO and OH, respectively (Toriseva et al. 1985). The 1.2-m Columbia Southern Millimeter-Wave Telescope at Cerro Tololo was used to map Cha I in the C¹⁸O ($J = 1 - 0$) (Toriseva et al. 1990) and the ¹²CO ($J = 1 - 0$) (Boulanger et al. 1998). Due to the small size of the telescope, the spatial resolution was moderate (9' HPBW). First observations in the 1' resolution range were obtained when the SEST telescope started observations in 1988. As the beam of the telescope is 45'' to 55'' at 3 mm, only small areas were mapped (Mattila et al. 1989). The Nagoya 4-m survey telescope, NANTEN, located at the Las Campanas Observatory, was used for mapping the Chamaeleon region in the ¹²CO, ¹³CO and C¹⁸O ($J = 1 - 0$) transitions (Mizuno et al. 2001; Mizuno et al. 1999; Mizuno et al. 1998). The beam size of the NANTEN telescope is 2.7 arcminutes but the observing grid was 8', 4' and 2', respectively.

This paper reports the mapping of the dense parts of the Cha I cloud in the C¹⁸O ($J = 1 - 0$) line with an angular resolution of 1'. These observations enable more detailed studies of the cloud structure than has been possible by using optical or NIR star counts (statistical limitations) or by the smaller size radio telescopes (diffraction limited beam sizes of several arc minutes). The relatively high frequency resolution of 43 kHz (corresponding to $\sim 0.12 \text{ km s}^{-1}$ at 109 GHz) makes it possible to extend the analysis also into the velocity space. An automated approach to data analysis, the "Clumpfind" routine developed by Williams et al. 1994, has been used to analyze the (x, y, v) data cube derived from the observations.

The observations and the data reduction are described in Sect. 2. In Sect. 3 we describe the cloud structure and results of the clump finding procedure, and discuss the new results in the light of previous observations concerning the signposts of star formation and magnetic fields in the cloud. A comparison with the NANTEN cores and clumps identified in this paper is presented in Sect. 4, and notes of some individual regions of special interest are presented in Sect. 5. In Sect. 6 we discuss the clump stability and mass spectrum. Finally, in Sect. 7 we summarize our conclusions.

2. Observations

The observations were conducted during various observing runs from 1988 to June 1996 using the Swedish-ESO-

Submillimetre-Telescope SEST on La Silla observatory in Chile. A 3 mm dual polarization single sideband (SSB) Schottky receiver in the frequency switching mode (with a throw of 7 MHz) was used to observe the $J = 1 - 0$ transitions of C¹⁸O, ¹³CO and C¹⁷O at 109, 110 and 111 GHz, respectively. The SEST high resolution, 2000 channel acousto-optical spectrometer with an 86 MHz bandwidth and a channel width of 43 kHz was split into two bands to measure the both polarizations simultaneously. The last C¹⁸O observations (1995,1996) were done using the SEST 3mm SSB SIS receiver.

Calibration was achieved by the chopper wheel method. As the observations are spread over many observing runs with different weather conditions the system temperatures varied accordingly. Typical values for the effective SSB system temperatures outside the atmosphere ranged from 350 K to 450 K (for the Schottky receiver) and from 200 K to 300 K (SIS receiver) for the C¹⁸O measurements, and from 300 K to 350 K for the ¹³CO measurements.

During the different runs the same reference position was always observed to monitor the calibration. Pointing was checked every 2-3 hours towards the nearby SiO maser source U Men. We estimate the pointing accuracy to have been better than 10'' during the observing runs. The focusing was done using a strong SiO maser.

C¹⁸O Altogether 1836 positions in the cloud were observed using a map step size of 1' and integration time of 60 seconds. The observations cover ~ 0.6 square degrees. The map is not fully sampled since the SEST beamsize at this frequency is 45''. We believe however that the clump detection is mainly limited by the noise level reached, and not by the slight under-sampling. The 1' step size corresponds to ~ 0.044 pc at the distance of 150 pc to the cloud. The (0, 0) position was arbitrarily chosen to coincide with star T39 near the cloud centre (J2000.0: 11^h09^m13^s.3, $-77^\circ 29' 12''$). The C¹⁸O observations of the Ced 110 and 112 regions have already been reported in Mattila et al. 1989.

The median RMS noise of the C¹⁸O spectra, after folding and baseline fit (typically second order baseline was used), is 0.1 K. Because of different observing conditions the noise goes occasionally up, and the maximum level is 0.22 K. For 90% of the spectra the RMS noise is smaller than 0.15 K.

The integrated C¹⁸O ($J = 1 - 0$) intensity map shown in Fig. 1 serves as a finding chart for the identified clumps (see Section 3) and some prominent objects in the cloud. The locations of the cores identified by Mizuno et al. 1999, and visible reflection nebulae Ced 110, Ced 111, and Ced 112, and the IRN are indicated. Also shown are the locations of two Class 0 sources (Cha-MMS1 and Cha-MMS2) detected by Reipurth et al. 1996. A velocity channel map over 20 channels of 0.12 km s^{-1} in width is shown Fig. 2. The velocities are indicated in the top of each panel.

¹³CO The central and southern parts of Cha I were observed in ¹³CO ($J = 1 - 0$). Observing was done in a similar manner as the C¹⁸O observations but with a 2' map step size. The number of observed positions is 296 and they cover an area of ~ 0.25 square degrees. The integrated T_A* map is shown in Fig. 3. The locations of Ced 110, Ced 111, and the IRN are also indicated.

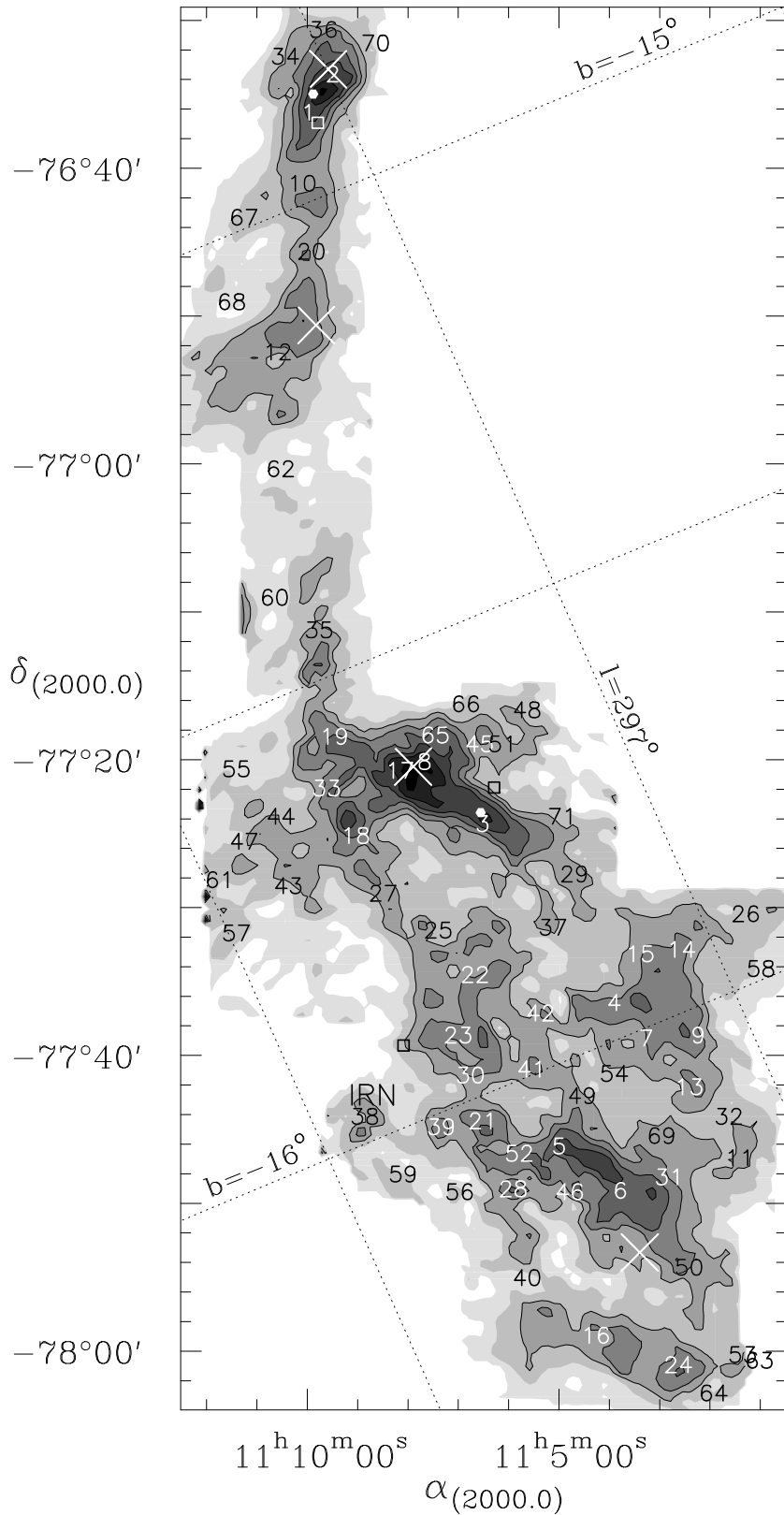


Fig. 1. Integrated $C^{18}O$ T_A^* intensity map over the LSR velocity range $2.9 - 5.9 \text{ km s}^{-1}$ of the Chamaeleon I cloud. The lowest greyscale level is 0.2 K km s^{-1} and the stepsize is 0.3 K km s^{-1} . The lowest contour level is 0.8 K km s^{-1} . The crosses indicate the positions of Mizuno et al. 1999 $C^{18}O$ cores 3, 4, 6 and 5 (from north to south). The locations of the reflection nebulae Ced 112, Ced 110 and Ced 111 (from north to south) are indicated with open squares. The locations of the Class 0 protostar candidates Cha-MMS1 and Cha-MMS2 are marked with filled circles. 'IRN' marks the location of the Infrared Reflection Nebula. The numbers identify the clumps found in the cloud (see Table. 1).

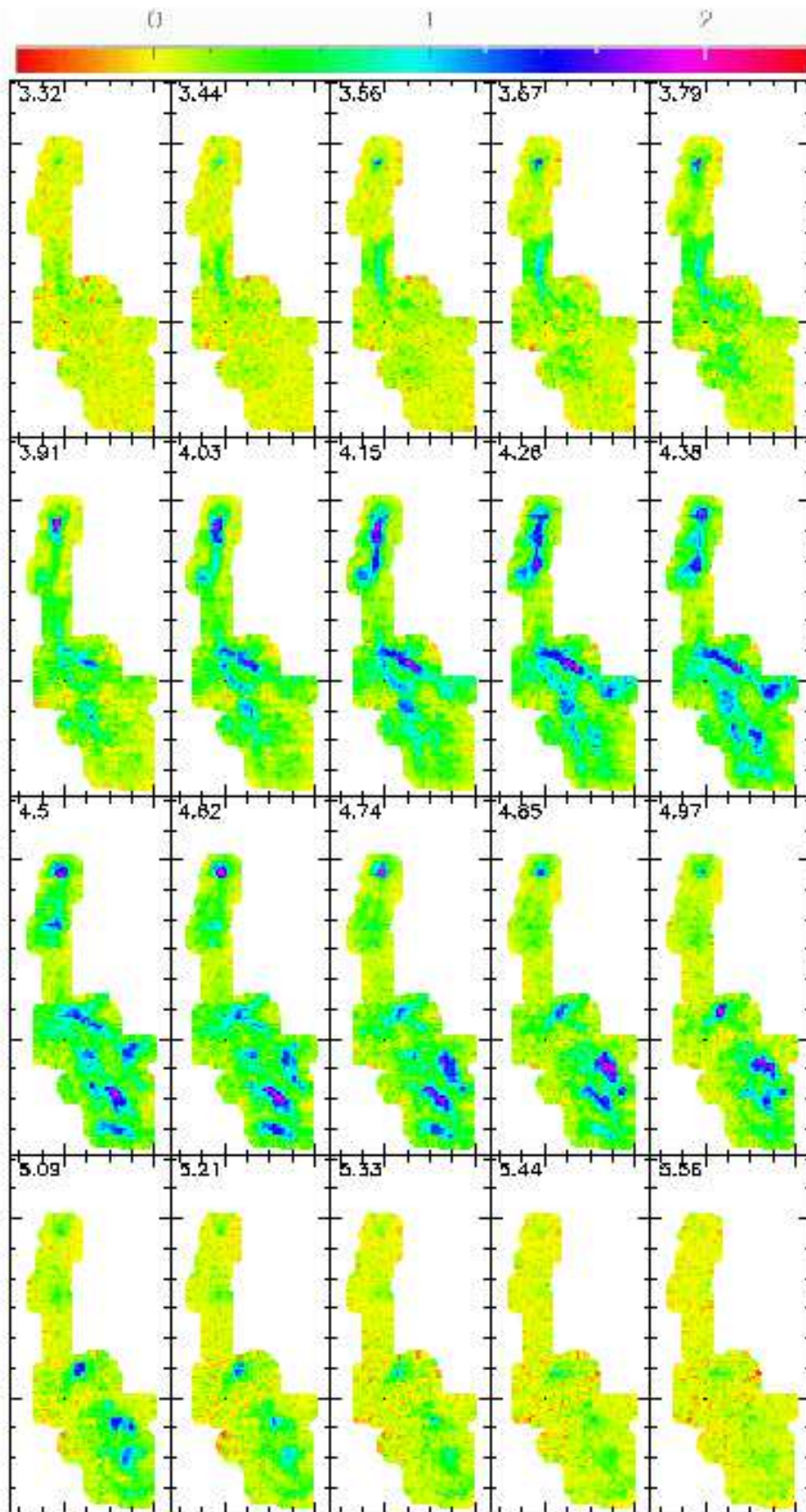


Fig. 2. Maps of the $C^{18}O$ T_A^* intensity in each of the central channels in the Chamaeleon I cloud. The LSR velocity in each panel is indicated in the upper corner of the panel. The highest intensity in the figure is ~ 2.2 K

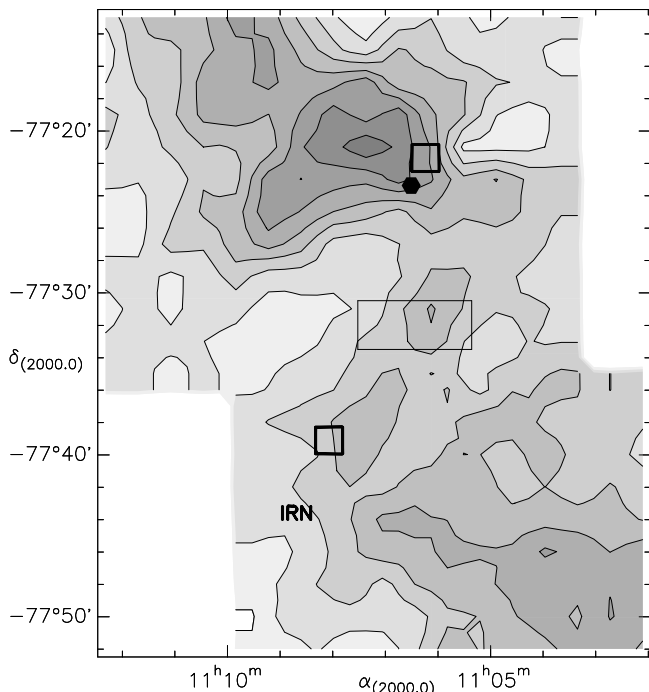


Fig. 3. The integrated $^{13}\text{CO}(J = 1 - 0)$ T_A^* intensity map of the central part of Cha I. The lowest greyscale level is 2.2 K km s^{-1} and the stepsize is 0.6 K km s^{-1} . The markers are the same as in Fig. 1. The box in the centre of the figure outlines the area displayed in Fig. 4.

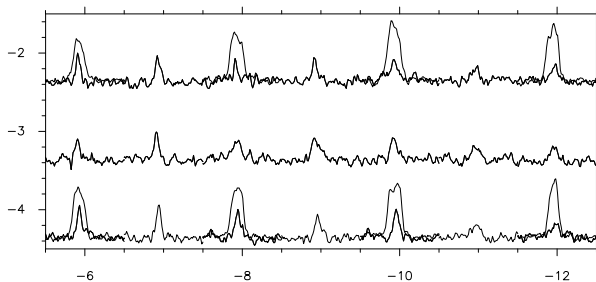


Fig. 4. Sample ^{13}CO and $\text{C}^{18}\text{O } J = 1 - 0$ spectra observed in a $6'$ by $2'$ region indicated in Fig. 3. The maximum $^{13}\text{CO } T_A^*$ in the figure is 3 K . The offsets relative to the map centre position (R.A. = $11^{\text{h}}09^{\text{m}}13^{\text{s}}.3$, Dec. = $-77^{\circ}29'12''$) in arc minutes are shown on the axes.

C¹⁷O Pointed $\text{C}^{17}\text{O}(J = 1 - 0)$ observations were made towards a few C^{18}O maxima. The integration time was 20 minutes, and the frequency throw was set to 12 MHz due to the hyperfine structure of the line. Longer C^{18}O integrations were made towards the same positions. In Fig. 5 we present C^{17}O and C^{18}O lines observed in three positions in the cloud.

3. The cloud structure

The integrated C^{18}O and $^{13}\text{CO}(J = 1 - 0)$ intensity maps presented in Fig. 1 and Fig. 3 show similar features on a

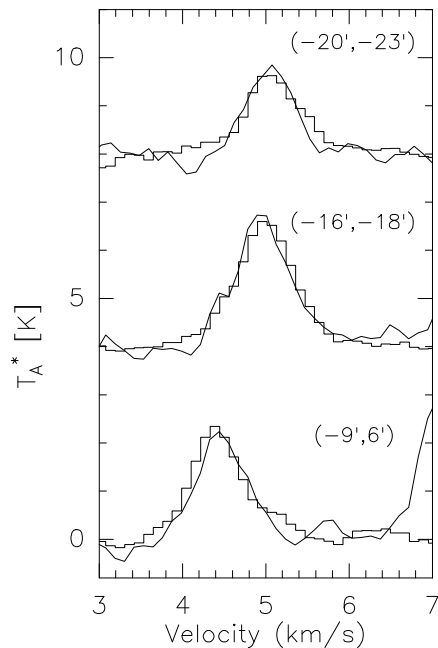


Fig. 5. A comparison of the $\text{C}^{18}\text{O}(J = 1 - 0)$ (histogram) and $\text{C}^{17}\text{O}(J = 1 - 0)$, $F = 5/2 - 5/2$ line (continuous line) intensities in selected C^{18}O maxima. The C^{17}O intensity has been multiplied by 9, which corresponds to the expected intensity ratio of the $\text{C}^{18}\text{O}(J = 1 - 0)$ line to this C^{17}O hyperfine component in the optically thin case.

large scale. As the ^{13}CO mapping was done using $2'$ step size it can not show the cloud structure in smaller detail. A closer look reveals significant differences between C^{18}O and ^{13}CO . For example, the extended C^{18}O maximum near $11^{\text{h}}03^{\text{m}}30^{\text{s}}$, $-77^{\circ}37'$ is not visible in the ^{13}CO map. Another example is given in Fig. 4: The intensities of the C^{18}O and $^{13}\text{CO}(J = 1 - 0)$ lines towards the shown positions do not correlate with each other. The reason for this failure is that the ^{13}CO line becomes optically thick in the direction of a high column density. The case of ^{12}CO is even worse as it is clearly strongly self absorbed in the line centre almost everywhere (see eg. Figures 3 and 19 in Mattila et al. 1989).

The comparison of the rare CO isotopomer C^{17}O and C^{18}O lines towards three positions in the cloud is shown in Fig. 5. The two transitions are well correlated and their intensity ratio (when the three $\text{C}^{17}\text{O}(J = 1 - 0)$ components are added) is 3.6, which corresponds to the abundance ratio in the local ISM (Wilson & Rood 1994). This comparison shows that both lines are likely to be optically thin and that the $\text{C}^{18}\text{O}(J = 1 - 0)$ line can be used to trace the total CO column density distribution.

A conspicuous feature in the C^{18}O maps is the presence of several clumpy filaments. The most prominent of these is the northern arm, a $40'$ long north-south oriented structure reaching down from Ced 112. In the centre and in the south, there are three almost parallel northeast-southwest oriented filaments, and an arc almost $40'$ in length, stretching from the neighbourhood of the IRN towards the northern arm. When investigated in detail these larger entities break up into smaller clumps.

The notable northeast-southwest oriented filaments break into small, often north-south oriented, clumps.

3.1. Clump identification

We have analyzed the small scale structure seen in the C¹⁸O map by using the automatic routine ‘‘Clumpfind’’ developed by Williams et al. 1994, which assumes that intensity maxima in the spectra correspond to localized density enhancements or ‘clumps’. The C¹⁸O ($J = 1 - 0$) spectral line map was interpolated to a three-dimensional $T_A^*(x, y, v)$ data cube, where the pixel size was 30'' in the position coordinates (one half of the map grid spacing), and one spectrometer channel width (0.12 km s^{-1}) in the radial velocity. The C¹⁸O emission from the cloud is confined to the velocity range $2.7 - 6.1 \text{ km s}^{-1}$ and only the central 29 channels corresponding to this range were included to the data cube. The maximum dimensions of the map in R.A. and Dec. directions are 41' and 96', respectively, and the dimensions of the data cube are $82 \times 192 \times 29$.

According to the analysis of Williams et al. 1994 the intensity stepsize, ΔT , for the Clumpfind routine should be set to two times the maximum noise level. Instead of the absolute maximum, we used here the ‘high’ value, 0.15 K, below which the noise level remains for 90% of the spectra, and accordingly the intensity stepsize was set to 0.3 K. This was used also as the intensity threshold for the clump search and the total cloud mass estimate.

With these parameters the Clumpfind routine identifies 71 clumps in the dataset. The data cube (‘‘ChaI.fits’’) and the clump identification file (‘‘ChaI.fits.clf’’), which is an output of the Clumpfind programme, will be made electronically available as FITS files. An IDL routine called ‘cl_surf.pro’ written by us to help in inspecting the cloud structure will also be available. This small programme shows clumps as isointensity surfaces in the (x, y, v) -space using the IDL Object Graphics and the ‘xObjView’ interface for zooming and rotating these surfaces.

The physical characteristics of the clumps are presented in Table 1. The columns of this Table are: (1) the clump identification number; (2) and (3) the Galactic coordinates of the clump centre of mass; (4) and (5) R.A. and Dec. (2000.0); (6) and (7) the LSR velocity of the line peak and the FWHM of the velocity dispersion in the clump; (8) the clump half-power radius; (9) the maximum C¹⁸O column density; (10) the clump mass with an error estimate based on the spectral noise; and (11) the ratio of the gravitational potential to kinetic energy in the clump. The numbering corresponds to order in decreasing peak intensity. Clumps 1–6 are detected at the level $7 \times \Delta T$ (14σ), clumps 7–13 at the level $6 \times \Delta T$, clumps 14–20 at the level $5 \times \Delta T$, clumps 21–36 at the level $4 \times \Delta T$, clumps 37–52 at the level $3 \times \Delta T$, and clumps 53–71 at the level $2 \times \Delta T$ (4σ).

The division of the data cube into clumps in the central and northern parts of the cloud is demonstrated in Fig. 6. The clumps identified by the Clumpfind routine are plotted in the figure as surfaces in the (x, y, v) space, where x and y are the R.A. and Dec. offsets from the $(0, 0)$ position, and v is the LSR velocity. The total velocity spread in Cha I is only 2.3 km s^{-1}

but sometimes two clumps can be separated along the same line of sight.

The C¹⁸O column densities (for each x, y, v pixel) were estimated by assuming optically thin emission, LTE with the excitation temperature $T_{\text{ex}} = 10 \text{ K}$, and a beam-source coupling efficiency, η_C , of 0.8 (half-way between η_{MB} and η_{Moon}). These were converted to mass column densities by assuming that the column density ratio $N(\text{C}^{18}\text{O})/N(\text{H}_2)$ is $2 \cdot 10^{-7}$ (Wilson & Rood 1994), and that the gas contains 10 % He. The masses were derived by summing up all pixels within a clump. The distance assumed in the mass calculation is 150 pc. For the gravitational potential energy estimates, it was assumed that the clump diameter in the radial direction (z) is equal to the smaller of the diameters in x and y directions. The mutual gravitational potential energies of all (x, y, z) pixel pairs were summed up and the internal potentials of pixels (small contribution) were added by approximating them with homogeneous spheres. The kinetic energies were also calculated pixel by pixel, and they include the contributions of systematic and turbulent motions and the internal thermal energy.

The total mass of the cloud (as traced by C¹⁸O above the threshold 0.30 K) is $230 M_{\odot}$. The derived clump masses range from 0.5 to $12 M_{\odot}$ with the median $2.9 M_{\odot}$. The geometric mean radii lie in the range $0.08 - 0.21 \text{ pc}$. The ratios of the gravitational to kinetic energies are between 0.1 and 1.2, and the median ratio is 0.4. The masses and the stability of the clumps will be briefly discussed in Sect. 6.

The largest uncertainty of the mass estimates is related to the $N(\text{C}^{18}\text{O})/N(\text{H}_2)$ conversion factor. The value we have used is close to those derived by Frerking et al. 1982 in Taurus and Harjunpää & Mattila 1996 in Cha I, and thereby also consistent with the factor used by Mizuno et al. 1999. The conversion factor is likely to change towards the centres of dense clumps due to CO depletion. However, as the column densities are generally modest in this cloud and most dramatic depletion effects are localized to very high density regions (e.g. Caselli et al. 1999) we believe that CO depletion does not cause significant errors to the clump statistics.

3.2. Star formation and cores

The locations of known and likely members and candidate pre-main-sequence stars of the Cha I Association are shown in Fig. 7, projected on the C¹⁸O molecular line map. The stellar objects were selected from Schwartz 1991 (Optical candidate members, black triangles), Persi et al. 2000 (known members with NIR excess (red squares), member candidates with NIR excess (open red triangles)), Cambr esy et al. 1998 (new Young Stellar Object candidates (asterisks)) and G omez & Kenyon 2001 (candidate pre-main-sequence stars (open circles)). Many of the objects listed in Schwartz 1991 were replaced by known members with NIR excess from Persi et al. 2000. A number of investigations have been conducted in the direction of the three reflection nebulae known to be locations of active star formation and more candidate members could be selected from them. We think, however,

Table 1. Clump properties.

No.	l ($^{\circ}$)	b ($^{\circ}$)	R.A. (2000) (h : m : s)	Dec. (2000) ($^{\circ}$: ' : ")	V_{LSR} (km s^{-1})	ΔV (km s^{-1})	Radius (pc)	$N(\text{C}^{18}\text{O})$ (10^{15} cm^{-2})	Mass (M_{\odot})	$ E_{\text{p}} /E_{\text{k}}$
1	297.04	-14.91	11:10:03.8	-76:36:18	3.8	0.6	0.15	1.9	5.1 (0.9)	0.9
2	297.00	-14.88	11:09:34.5	-76:33:43	4.6	0.6	0.14	2.0	5.2 (0.8)	1.0
3	297.18	-15.72	11:06:30.0	-77:24:18	4.3	0.7	0.19	2.1	11.7 (2.2)	1.1
4	297.14	-15.96	11:03:50.3	-77:36:24	4.9	0.6	0.12	1.6	4.5 (0.8)	0.8
5	297.26	-16.09	11:04:54.9	-77:46:08	4.6	0.6	0.12	1.7	4.0 (0.7)	0.7
6	297.22	-16.16	11:03:40.8	-77:49:04	4.5	0.6	0.17	2.0	10.1 (1.6)	1.2
7	297.12	-16.01	11:03:09.9	-77:38:44	4.9	0.5	0.11	1.4	3.7 (0.6)	0.8
8	297.22	-15.63	11:07:39.6	-77:20:09	5.0	0.7	0.17	1.6	6.9 (1.3)	0.8
9	297.06	-16.03	11:02:07.4	-77:38:34	4.9	0.5	0.11	1.3	2.8 (0.5)	0.8
10	297.08	-14.98	11:10:10.7	-76:41:05	4.1	0.5	0.17	1.3	5.9 (1.2)	1.1
11	297.08	-16.18	11:01:17.2	-77:46:52	4.9	0.5	0.13	1.0	2.6 (0.6)	0.6
12	297.19	-15.14	11:10:40.1	-76:52:31	4.3	0.6	0.22	1.4	11.6 (2.4)	1.0
13	297.10	-16.08	11:02:18.0	-77:42:03	4.7	0.5	0.11	1.3	2.7 (0.5)	0.8
14	297.04	-15.94	11:02:28.6	-77:32:44	4.4	0.5	0.17	1.1	5.8 (1.1)	1.0
15	297.08	-15.93	11:03:17.7	-77:33:05	4.7	0.5	0.14	1.0	2.6 (0.5)	0.5
16	297.31	-16.30	11:04:09.1	-77:58:56	4.6	0.6	0.21	1.2	9.1 (2.2)	0.9
17	297.25	-15.63	11:08:09.5	-77:20:46	4.3	0.7	0.14	1.5	5.7 (1.0)	0.7
18	297.32	-15.68	11:09:02.2	-77:25:10	4.0	0.9	0.14	2.0	5.4 (1.3)	0.5
19	297.30	-15.57	11:09:29.1	-77:18:32	4.1	0.8	0.14	1.7	5.5 (1.2)	0.6
20	297.10	-15.05	11:10:00.2	-76:45:44	4.3	0.5	0.13	1.3	2.9 (0.7)	0.6
21	297.33	-16.03	11:06:26.9	-77:44:26	4.5	0.6	0.14	1.4	3.4 (0.8)	0.5
22	297.26	-15.87	11:06:37.6	-77:34:30	4.5	0.8	0.16	1.4	6.7 (1.5)	0.6
23	297.31	-15.93	11:06:58.4	-77:38:41	4.1	0.7	0.15	1.5	5.2 (1.1)	0.7
24	297.25	-16.36	11:02:29.7	-78:00:55	4.7	0.7	0.13	1.4	4.2 (1.0)	0.5
25	297.28	-15.81	11:07:22.9	-77:31:31	4.1	0.6	0.16	1.2	4.5 (1.1)	0.6
26	296.96	-15.93	11:01:11.8	-77:30:23	4.3	0.4	0.12	0.7	2.7 (0.6)	0.6
27	297.32	-15.75	11:08:28.9	-77:29:08	4.0	0.6	0.14	1.1	3.4 (0.9)	0.6
28	297.33	-16.11	11:05:50.8	-77:49:02	4.4	0.7	0.12	1.4	3.1 (0.7)	0.5
29	297.11	-15.81	11:04:38.7	-77:27:44	4.3	0.6	0.17	0.9	4.7 (1.2)	0.6
30	297.32	-15.98	11:06:42.1	-77:41:22	3.9	0.5	0.12	1.0	1.9 (0.5)	0.5
31	297.16	-16.17	11:02:41.1	-77:48:10	5.1	0.6	0.17	0.9	5.4 (1.2)	0.7
32	297.07	-16.13	11:01:30.6	-77:44:03	4.6	0.4	0.09	0.7	1.1 (0.3)	0.4
33	297.33	-15.62	11:09:37.9	-77:21:59	4.1	0.9	0.11	1.6	3.2 (0.7)	0.4
34	297.04	-14.84	11:10:32.6	-76:32:33	4.6	0.6	0.08	0.9	1.2 (0.3)	0.3
35	297.27	-15.45	11:09:47.2	-77:11:19	3.7	0.6	0.19	1.2	5.4 (1.4)	0.6
36	296.99	-14.83	11:09:45.2	-76:30:40	4.5	0.7	0.10	1.1	1.8 (0.4)	0.4
37	297.16	-15.86	11:05:04.0	-77:31:19	5.0	0.7	0.16	0.6	3.2 (1.0)	0.4
38	297.44	-15.97	11:08:49.0	-77:44:13	4.3	0.6	0.14	1.0	2.6 (0.8)	0.5
39	297.37	-16.01	11:07:17.6	-77:44:50	3.9	0.6	0.13	1.1	2.3 (0.6)	0.4
40	297.36	-16.21	11:05:33.2	-77:55:02	4.4	0.7	0.18	1.0	4.2 (1.3)	0.4
41	297.25	-16.00	11:05:28.6	-77:40:56	4.3	0.8	0.10	1.3	2.2 (0.6)	0.3
42	297.22	-15.94	11:05:18.6	-77:37:08	4.4	0.9	0.13	0.7	3.3 (0.9)	0.3
43	297.42	-15.70	11:10:23.6	-77:28:35	4.3	0.7	0.15	0.6	3.3 (1.0)	0.4
44	297.39	-15.63	11:10:33.0	-77:23:57	4.5	0.7	0.11	1.0	2.3 (0.6)	0.4
45	297.15	-15.64	11:06:32.8	-77:19:00	4.5	0.7	0.11	0.8	2.1 (0.5)	0.3
46	297.27	-16.14	11:04:41.7	-77:49:14	4.0	0.5	0.12	0.7	1.8 (0.5)	0.4
47	297.44	-15.64	11:11:17.4	-77:25:40	4.5	0.7	0.09	1.0	1.3 (0.4)	0.3
48	297.08	-15.62	11:05:37.0	-77:16:38	4.5	0.7	0.11	0.9	1.7 (0.5)	0.3
49	297.21	-16.04	11:04:27.9	-77:42:41	4.4	0.8	0.12	1.1	2.5 (0.7)	0.3
50	297.19	-16.27	11:02:16.7	-77:54:18	4.9	0.9	0.18	0.9	6.0 (1.8)	0.4
51	297.13	-15.65	11:06:05.1	-77:18:58	4.7	0.6	0.12	0.4	1.2 (0.4)	0.2
52	297.30	-16.08	11:05:43.3	-77:46:36	3.9	0.5	0.10	0.7	1.1 (0.3)	0.4
53	297.18	-16.38	11:01:11.9	-78:00:11	5.2	0.5	0.12	0.7	1.4 (0.4)	0.4
54	297.17	-16.04	11:03:48.1	-77:41:10	4.0	0.6	0.11	0.4	1.0 (0.4)	0.2
55	297.42	-15.56	11:11:27.2	-77:20:45	4.4	0.6	0.13	0.4	1.6 (0.6)	0.2
56	297.38	-16.09	11:06:54.3	-77:49:15	4.3	0.5	0.11	0.5	0.8 (0.3)	0.2
57	297.49	-15.73	11:11:25.7	-77:31:51	4.0	0.6	0.09	0.4	0.7 (0.3)	0.1
58	296.97	-16.00	11:00:53.3	-77:34:05	4.3	0.4	0.10	0.4	0.6 (0.2)	0.2
59	297.43	-16.05	11:08:02.3	-77:48:05	4.3	0.6	0.10	0.5	0.9 (0.3)	0.2
60	297.30	-15.40	11:10:42.5	-77:09:09	3.8	0.6	0.14	0.6	1.6 (0.6)	0.2
61	297.49	-15.67	11:11:46.7	-77:28:15	4.1	0.7	0.08	0.5	0.8 (0.3)	0.2
62	297.24	-15.26	11:10:35.9	-77:00:28	3.9	0.8	0.22	0.4	3.8 (1.4)	0.2
63	297.17	-16.39	11:00:52.0	-78:00:35	4.5	0.4	0.10	0.4	0.7 (0.2)	0.2
64	297.23	-16.41	11:01:46.2	-78:02:48	4.7	0.5	0.08	0.4	0.6 (0.2)	0.2
65	297.19	-15.61	11:07:27.9	-77:18:22	3.7	0.7	0.11	0.6	0.5 (0.2)	0.1
66	297.15	-15.59	11:06:51.0	-77:16:17	4.5	0.7	0.07	0.7	0.7 (0.2)	0.2
67	297.16	-14.99	11:11:21.6	-76:43:23	4.7	0.5	0.10	0.5	0.7 (0.3)	0.2
68	297.21	-15.07	11:11:35.4	-76:49:07	4.5	0.5	0.14	0.2	1.4 (0.5)	0.3
69	297.15	-16.12	11:02:51.2	-77:45:21	4.1	0.5	0.13	0.4	1.2 (0.4)	0.3
70	296.94	-14.87	11:08:43.2	-76:31:35	4.4	0.7	0.10	0.3	0.8 (0.3)	0.2
71	297.10	-15.75	11:04:52.7	-77:23:48	3.9	0.8	0.12	0.7	1.0 (0.4)	0.1

that the objects indicated in Fig. 7 reflect well the general distribution of young stellar objects in Cha I.

Concentrations of young stars are seen in the direction of the three reflection nebulae, Ced 112 in the north, Ced 110 in the centre, and Ced 111 near IRN. The stellar clusters near Ced 112 and Ced 110 are associated with massive molecular clumps. Besides the immediate surroundings of Ced 112 and Ced 110, also the most prominent molecular filaments in the northern and central parts of the cloud, i.e. the Northern arm, the 40' Arc, and the central filament near Ced 110, are lined

with young stars. This suggests that these stellar groupings and large scale molecular structures have a common origin.

In contrast to the situation near the two other reflection nebulae, clumps around Ced 111 and the IRN belong to the least massive in the cloud, and it seems that most of the molecular material around young stars has dispersed on this side of the cloud.

In the southern parts, south of the galactic latitude $-16^{\circ}05'$, the surface density of stars is clearly lower than elsewhere in the cloud. In particular, there is only one ISOCAM mid-IR excess member candidate source and significantly fewer

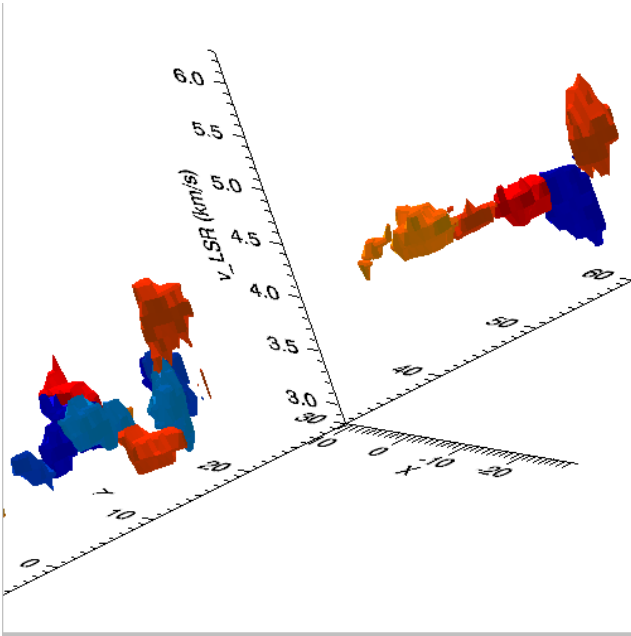


Fig. 6. Clumps in the central and northern part of Cha I. Output of the `cL_surf` routine. Each clump identified with the `Clumpfind` programme is shown as an isointensity surface in the (x, y, v) space. Different colours are used to help in distinguishing between separate clumps. The intensity level chosen for this figure is $T_A^* = 1$ K. The x and y axes represent the offset in arcminutes from the map centre (R.A. = $11^{\text{h}}09^{\text{m}}13^{\text{s}}.3$, Dec. = $-77^{\circ}29'12''$), and the v axis represents the LSR velocity in km s^{-1} . Note the large velocity gradient between the two northernmost clumps 1 and 2 at $y \approx 55'$ (here on the right, the viewing angle makes the y -offsets look larger) and the exceptionally large velocity of clump 8 in the centre at $y \approx 10'$ (here on the left).

NIR member candidates than in the north. It should be noted, however, that the ISOCAM observations did not go below $\sim -77^{\circ}47'$. The two parallel southern filaments were detected in FIR surface emission by Haikala et al. 1998 and Tóth et al. 2000. Considering the small number of NIR and mid-IR sources, these structures are likely to be cold and their clumps are possibly in their pre-star formation stage. (The same might be true for the starless clump (12) south of Ced 112, even though it lies next to a string of young stars on its eastern side.)

The large number of newly born stars and their concentration around filaments seen in the molecular line map indicate efficient compression of gas and subsequent star formation. According to the hydrodynamical models (e.g. Klessen 2001), these features are characteristic of cloud fragmentation in the conditions of little turbulent support (decaying turbulence), or turbulence driven by large-scale shocks. In contrast, turbulent support driven on small scales leads to inefficient and dispersed birth of stars. The modest $C^{18}O$ column densities, the fairly large fraction of visible stars amongst the associated YSOs, and

the fact that only two protostar candidates have been found in the cloud, suggest on the other hand that we are witnessing the aftermath of star formation. The total mass of the young stars associated with the cloud has been estimated to be about $120 M_{\odot}$ (Mizuno et al. 1999), which corresponds to about 50% of the mass of high column density gas traced by $C^{18}O$.

3.3. Orientation of the magnetic fields

Near-infrared (H -band) polarimetry of heavily reddened background stars and embedded objects was used by McGregor et al. 1994 to study the magnetic field structure in Cha I. The stellar polarization due to aligned dust particles in the direction of the cloud is illustrated in Fig. 8. The data is from McGregor et al. 1994 and Whittet et al. 1994. The polarizations of some of the Cha I members are influenced by intrinsic polarization due to scattering in the circumstellar dust or the surface of the molecular cloud. Depending on the geometry, this can lead to depolarization and/or rotation of the polarization direction. A notable example is the IRN (polarization not plotted in Fig. 8) for which the H band polarization is 33% and the polarization angle differs by tens of degrees from the cloud average (McGregor et al. 1994). The small foreground reddening in the direction of Cha I and the high galactic latitude makes it certain that the observed high polarizations are in major part due to dust in the Chamaeleon region. These observations probe magnetic fields in the obscured parts of the cloud and have thus a direct bearing on structures revealed by the present $C^{18}O$ mapping. The polarization field is well ordered throughout the cloud, changing its orientation from nearly E-W in the northern part to NW-SE in the centre and in the south. This orientation, which is consistent with the large-scale polarization field in the region (Whittet et al. 1994), is roughly perpendicular to the cloud axis, the dense filaments seen in $C^{18}O$ and presumably also to the magnetic field in the region. As pointed out by McGregor et al. 1994, the assumed orientation of the magnetic field suggests that it has steered the cloud collapse preferentially along the field lines. That also dense filaments seem to be oriented at right angles to this magnetic field lends support to this view.

It should be noted, furthermore, that turbulent fragmentation models predict that the resulting magnetic field in dense filaments or sheets is parallel to the direction of elongation, because this magnetic field component is amplified in shocks (Padoan & Nordlund 2002). The H -polarization percentage versus visual extinction in Cha I seems to saturate at $A_V \sim 7$ (see Fig. 4 of McGregor et al. 1994), suggesting that the grain alignment weakens in the densest parts (see the discussion in Goodman et al. 1992).

4. Comparison with NANTEN cores

The integrated $C^{18}O$ ($J = 1 - 0$) intensity map presented in Fig. 1 shows the same general outline as the one taken with the 4-m NANTEN telescope (Mizuno et al. 1999). As expected, the higher spatial resolution of the SEST allows one to resolve more details. The cores detected by Mizuno et al. 1999

are all seen in the SEST data but these cores are fragmented into smaller entities, both spatially and in velocity.

The correspondence between 'cores' identified by Mizuno et al. 1999 in the NANTEN map, and 'clumps' identified with the Clumpfind programme in the SEST map is most clear in the northern arm or Cha I North. Our clumps 1 and 2 in Cha I North with a total mass of about $10 M_{\odot}$ correspond to the centre of NANTEN core 3 (N3), for which they derived the mass $29 M_{\odot}$. The velocity difference between clumps 1 and 2 is clearly visible in Fig. 6 (at $y \approx 55'$). Clump 12 ($12 M_{\odot}$) about $15'$ south of Cha I North corresponds to core N4 ($16 M_{\odot}$). The SEST map shows, however, several subsidiary peaks also in the north, and especially the windswept shape of the northern filament is clearly visible there.

In Cha I Centre and in the southern part of the cloud, where the structure is more complex, the two NANTEN cores (6 and 5) decompose into several clumps. Towards the absolute intensity maximum of the cloud, the peak of core N6, two clumps lie in the line of sight at different radial velocities (clumps 8 and 17 at $y \approx 10'$ in Fig. 6). The existence of two velocity components was already noted by Mizuno et al. 1999. Besides these two, core N6 comprises two major clumps (3, 19) and has several smaller clumps on its western side. The total mass of the four most massive clumps is $30 M_{\odot}$, which roughly corresponds to the mass derived for Mizuno's core 6, $39 M_{\odot}$.

The centre of core N5 in the south correspond to our clumps 5 and 6 which belong to one of the two parallel filaments in the south¹. The procedure we have used identifies half a dozen of clumps in this filament with a total mass of $30 M_{\odot}$, which is well below the mass derived for core N5 ($82 M_{\odot}$) by Mizuno et al. 1999. The most massive individual clumps in the two southern filaments are numbers 6 and 16, respectively, which also are among the most massive in the whole cloud.

5. Notes on individual regions

5.1. Cha I North

The Clumpfind program finds in this region three major clumps, 1, 2, 10. Clump 1 is in the direction of the B9V star HD97300, which is the illuminating source of Ced 112. Clump 2 corresponds to the opaque core described in Jones et al. 1985. It contains the Class 0 protostar candidate Cha-MMS2 (Reipurth et al. 1996), which is a possible driving source of the molecular outflow detected in this region (Mattila et al. 1989). Cha-MMS2 lies in the apex of the blueshifted outflow lobe. Numerous mid-IR sources with mid-IR excess are seen projected in the line of sight to clumps 1 and 2 (Persi et al. 1999; Persi et al. 2000). One of these sources, ISOCAM-ChaINa2 has a SED characteristic of a Class I source and has been proposed by Persi et al. 1999 to be the possible exciting source of the molecular outflow.

Clump 12 (the centre of N4), which lies $15'$ south of clumps 1 and 2 is devoid of mid-IR sources and does not seem to

¹ Note: The coordinates of clump 5 in Table 1. of Mizuno et al. 1999 are not correct. The correct coordinates are $l, b = 297^{\circ} 23, -16^{\circ} 13$ (Mizuno 2003, private communication.)

be connected with star forming activity. This core was detected also in the ISOPHOT $170 \mu\text{m}$ serendipity survey of the Chamaeleon clouds (Tóth et al. 2000), which indicates the presence of very cold dust in this clump.

5.2. Cha I Centre

The prominent intensity maximum near Ced 110 (N6) is split into four major clumps: 3, 8, 17 and 19. Projected on the sky, clump 8 partially overlaps with clump 17, but it has a larger radial velocity (see Fig 6). This region contains a cluster of low-mass young stellar objects which have been studied extensively in recent years (e.g. Prusti et al. 1991; Persi et al. 2000; Persi et al. 2001; Lehtinen et al. 2001; Lehtinen et al. 2003). The dense dust ridge detected at $200 \mu\text{m}$ with ISOPHOT (Lehtinen et al. 2001) coincides with the central parts of clumps 3 and 8. The Class 0 candidate Cha-MMS1 (Reipurth et al. 1996) is probably embedded in clump 3, close to its north-eastern boundary. Reipurth et al. 1996 suggested that Cha-MMS1 is the central source of the bipolar molecular outflow discovered by Mattila et al. 1989, whereas Lehtinen et al. 2003 regarded the Class I infrared source IRS 4 as a more likely candidate. In the latter case the outflow would originate between clumps 3 and 17.

The clumps 60, 35, 19, 33, 18, 27 and 25, together with the clumps west of the Ced 111 region, 22, 23 and 30, form a nearly continuous arc of $40'$. The clumps in the arc are however readily separated both spatially and in velocity (Fig. 2).

5.3. Ced 111 region

Besides the Ced 111 reflection nebula, the southeastern edge of the cloud contains the IRN and several pre-main-sequence stars (eg. Schwartz 1991). Only four clumps, 22, 23, 30 and 38 are located in the region which has formerly been a centre of active star formation. It seems that this process has consumed and dispersed most of dense material of the ambient cloud. The clump 38, which is detected at a low level, is associated with the IRN.

5.4. Cha I West and South

The clumps 4, 7, 9, 13, 14 and 15 to the West of Ced 111 form a massive condensation of clumps. This conglomeration of clumps is probably associated with the Very cold Core 5 (VCC5) in Tóth et al. 2000. The two parallel elongated structures to the the South are clearly seen in the far-IR (Haikala et al. 1998, Tóth et al. 2000). Tóth et al. 2000 designated these structures as VCC4 and VCC3. Similar to VCC4 also the two other separate into smaller units. The clumps 5 and 6 correspond to VCC4 and clumps 16 and 24 to VCC3. None of these structures contain IRAS point sources with colours typical of newly born stars, and seem to have no active star formation. The ISOCAM mid-IR Chamaeleon mapping (Persi et al. 2000) covered only the northern part of these regions.

6. Distribution of clump masses and their stability

The distributions of the derived clump masses, the ratios of the potential to kinetic energies, and the ratios of the thermal to turbulent kinetic energies are shown in Fig. 9. The clump masses range from 0.6 to 12 M_{\odot} with the median 2.7 M_{\odot} . The $|E_{\text{pot}}|/E_{\text{kin}}$ ratios are between 0.1 and 1.2, and the median ratio is 0.4. The ratio is close to unity for the most massive clumps. For most clumps the turbulent energy dominates over the thermal energy.

As the condition of the virial equilibrium (in the absence of an external pressure) is $|E_{\text{pot}}|/E_{\text{kin}} = 2$, the result indicates that, strictly speaking, none of the clumps identified here is a gravitationally bound entity. They are either dissolving or stabilized by the outside pressure due to interclump turbulence or by magnetic fields.

We may estimate for each clump a hypothetical external pressure, P_{ext} , required to balance the 'extra' turbulent motions using the virial equilibrium equation:

$$2E_{\text{kin}} + E_{\text{pot}} = 4\pi R^3 P_{\text{ext}}. \quad (1)$$

The distribution of these 'equilibrium pressures' is shown in Fig. 10. The distribution is asymmetric, peaking towards a minimum which lies close to the value 10^{-12} Pa ($P/k \sim 7 \cdot 10^4$ cm⁻³K). From observational statistics it is likely that the external pressure may be sufficient to stabilize some of the clumps, but not to force any of them to collapse. In case the pressure of the interclump medium is roughly constant across the cloud, the minimum of the derived P_{ext} values should correspond to the actual interclump pressure. One can see in Fig. 10 that in fact for about 40 clumps P_{ext} is close to 10^{-12} Pa. We assume therefore that this value represents the typical interclump pressure, and that those 40 clumps are in the virial equilibrium. The mass distribution of these 40 clumps is presented as hatched columns in Fig. 9. It is similar to that of the original sample, but these clumps have less marked turbulent motions (see the bottom panel of Fig. 9). In case the clumps are stabilized by the magnetic field, the field strength is 16 μG , as can be obtained from the following formula for the magnetic pressure: $P_{\text{m}} = B^2/8\pi = 10^{-13}$ Pa.

The clump mass spectrum can be, in principle, used for studying the mechanisms of cloud fragmentation, and, if sufficiently small scale structures can be resolved, also for predicting the stellar initial mass function, IMF (see e.g. Padoan & Nordlund 2002; Ballesteros-Paredes & Mac Low 2002; Klessen 2001). The spatial resolution and the RMS noise level of the present data are clearly not sufficient for studying the complete mass spectrum down to clumps at $\leq 0.5 M_{\odot}$. Stars may form in the interiors of the larger, quasi-stable clumps identified here, but the relation between their masses and the stellar mass function is beyond the scope of this paper.

We discuss briefly, however, the possibility to understand the mass spectrum of the hypothetically virialized clumps in terms of the turbulent fragmentation model presented in Padoan et al. 1997 and Padoan & Nordlund 2002. These studies predict 1) the mass distribution of dense cores, 2) the proba-

bility density function of the gas density, and 3) the subsequent mass distribution of collapsing clumps arising from supersonic turbulence.

In the model of Padoan & Nordlund 2002 the mass distribution of *all* clumps follows a power law depending on the power spectrum of the turbulence: $N(m) \propto m^{-3/(4-\beta)}$, where β is the spectral index of the turbulence (see their Eqs. (5) and (18)). Using their assumption that the density and mass distributions are statistically independent, one can derive the distributions of the Jeans' masses, $\Phi_J(m)$, or alternatively, the distribution of 'equilibrium masses' $\Phi_E(m)$, under the condition of constant external pressure expressed in Eq. 1. In the latter case the equivalent of Eq. (24) of Padoan & Nordlund 2002 can be written as:

$$\Phi_E(m) \propto m^{-3/(4-\beta)} \int_{\tilde{m}=0}^m g(\tilde{m}) d\tilde{m}, \quad (2)$$

where $g(\tilde{m})$ is the probability density function of equilibrium masses, and \tilde{m} is the variable of integration. The function g is derived below. The observed distribution of pressure balanced clumps (in the top of Fig. 9) should be a sample of the distribution Φ_E .

The β -index should be reflected in the observed size-linewidth relation, $\Delta v \propto R^{\alpha}$, since $\alpha = (\beta - 1)/2$ according to Eq.(13) of Padoan & Nordlund 2002. The expected values range from 1.6 (for incompressible turbulence) to 2 (shock dominated turbulence; Larson 1979; Larson 1981). The clumps identified in the present study show a very weak dependence between the line width and size, and a large scatter. A least-squares fit to the identified clumps gives $\alpha = 0.16 \pm 0.09$ (instead the usual $\alpha \approx 0.5$) with a small correlation coefficient of $r = 0.2$. The AOS channel width and the mapping step size correspond to 0.12 km s⁻¹ and 0.044 pc, respectively. These values correspond to a large fraction of the total range of the observed line widths (from 0.4 to 0.9 km s⁻¹) and sizes (from 0.08 to 0.22 pc). Therefore, even if a correlation between the line widths and clump sizes exists in the cloud, the present data are not suitable to make a meaningful fit when the errors are taken into account. The qualitative results presented here do not depend, however, strongly on the actual value of β . Since its determination from observations is furthermore subject to large uncertainties, we assume in the following the value 2 valid for compressible turbulence.

We next derive the function $g(m)$ appearing on the right hand side of Eq. 2. According to the turbulent fragmentation models of Padoan et al., the probability density distribution of the local density parameter, $p(x)$, where $x \equiv n/\bar{n}$, and \bar{n} is the average number density in the cloud, follows approximately a lognormal function. The probability density distribution *per unit mass*, i.e. the mass function at any given density, $f(x) = xp(x)$, can then be written as

$$f(x) = \frac{1}{\sqrt{2\pi}\sigma_{\ln x}} \exp\left\{-\frac{1}{2}\left(\frac{\ln x - \overline{\ln x}}{\sigma_{\ln x}}\right)^2\right\}. \quad (3)$$

(see Eqs. (1) and (7) of Padoan et al. 1997). As pointed out in the latter study, the properties of the lognormal function and the selection of the variable x such that $\bar{x} = 1$ imply

that the mean, $\overline{\ln x}$, and the standard deviation, $\sigma_{\ln x}$, are related by $\overline{\ln x} = -\sigma_{\ln x}^2/2$. The distribution is thus characterized by a single parameter, $\sigma_{\ln x}$. This in turn depends on the rms Mach number, \mathcal{M} , of the turbulent flow according to $\sigma_{\ln x}^2 \approx \ln(1 + 0.25\mathcal{M}^2)$ (Padoan et al. 1997, Eq. (9)), i.e. inhomogeneity grows with the speed of the flow.

Turning to a small element of the cloud, we examine an isothermal, homogeneous clump formed within it. From Eq. 1 one can derive the following expression for the mass of a spherical, virialized clump as a function of the density parameter x :

$$m(x) = ax^{-1/2}(b - cx^{-1})^{3/2}, \quad (4)$$

where

$$\begin{aligned} a &\equiv \left(\frac{5}{G}\right)^{3/2} \left(\frac{3}{4\pi\mu\bar{n}}\right)^{1/2} \\ b &\equiv \frac{kT}{\mu} + \sigma_v^2 \\ c &\equiv \frac{P_{\text{ext}}}{\mu\bar{n}}, \end{aligned} \quad (5)$$

where G is the gravitational constant, k is the Boltzmann constant, T is the gas kinetic temperature, μ is the mean molecular mass, and σ_v is the turbulent velocity dispersion inside the clump. For Jeans' masses the corresponding function can be written as $m_j(x) = (\frac{3}{4})^{3/2} ab^{3/2} x^{-1/2}$ with the same definitions of a and b as in Eq. 5. One can see from Eq. 4 that a minimum density, $x_0 = c/b$, is required for an equilibrium mass. This condition is equivalent with the requirement that the internal pressure, $P_{\text{int}} \equiv n\mu(kT/\mu + \sigma_v^2)$, must be equal to or larger than P_{ext} . The equilibrium mass reaches a maximum at $x = 4x_0 = 4c/b$, where $m = (3^{3/2}/16) ab^2 c^{-1/2}$, and decreases monotonically thereafter. At the maximum $m(x) = m_j(x)$ and $E_{\text{pot}} = -\frac{3}{2}E_{\text{kin}}$. This turning point signifies the density at which gravity starts to dominate over external pressure as the counterforce against the internal pressure.

The functions $m(x)$ and $m_j(x)$ are plotted in Fig. 11a. The kinetic temperature is assumed to be 10 K, and the average gas density and velocity dispersion derived for the C¹⁸O clumps ($\bar{n} = 5500 \text{ cm}^{-3}$, $\sigma_v = 260 \text{ ms}^{-1}$) are used to estimate the values of the parameters a , b and c . It can be seen from this figure that $m(x)$ exceeds $m_j(x)$ when $x > 4c/b$. According to the definition of Jeans' mass this means that the equilibrium masses on the right hand side of the maximum will collapse if the external pressure increases.

The probability density function of equilibrium masses, $g(m)$, can be derived from Eqs. 3 and 4. For each mass below the maximum derived above there are two possible values of the density parameter x , say x_1 (low density, $< 4x_0$) and x_2 (high density, $> 4x_0$, $4x_0$ corresponds to about 10^4 cm^{-3} with the parameters used for Fig. 11).

If we denote by M and X the random variables describing the mass and the density parameter, respectively, the probability distribution function of the mass can be expressed with the aid of the density as follows:

$$\begin{aligned} P(M \leq m) &= P(X \leq x_1) + P(X \geq x_2) \\ &= \int_0^{x_1(m)} f(x)dx + \int_{x_2(m)}^{\infty} f(x)dx. \end{aligned} \quad (6)$$

The probability density function, $g(m)$ can then be obtained from the latter by derivation:

$$\begin{aligned} g(m) &= f(x_1(m)) \frac{dx_1(m)}{dm} - f(x_2(m)) \frac{dx_2(m)}{dm} \\ &= \frac{f(x_1(m))}{m'(x_1(m))} - \frac{f(x_2(m))}{m'(x_2(m))}, \end{aligned} \quad (7)$$

where function f is defined by Eq. 3, $x_1(m)$ and $x_2(m)$ are the inverse functions of $m(x)$ in the regions $x_0 \leq x \leq 4x_0$ (low densities) and $x > 4x_0$ (high densities), respectively, and m' is the derivative of function m . The expressions of $x_1(m)$ and $x_2(m)$ that follow directly from Eq. 4 are rather intricate and they are not shown here. The functions $x_1(m)$ and $x_2(m)$ are, however, plotted in Fig. 11b, together with the inverse of Jeans' mass, $x_j(m)$.

Estimates for the parameters a , b , c and β in Eqs. 4 and 2 can be derived from observations or, as in the case of β , from theoretical predictions. The mass distributions of equilibrium and collapsing clumps predicted by the model of Padoan et al. depend then ultimately on the gas density distribution described by the parameter $\sigma_{\ln x}$. It turns out that a small dispersion in densities ($\sigma_{\ln x} < 1.2$) makes the Jeans' mass distribution peak towards high masses, $M > 10M_{\odot}$, which contradicts the observed stellar mass distribution in Cha I and in other dark clouds. A situation where both Jeans' masses and equilibrium clump masses peak below $1 M_{\odot}$ require a wide range of densities, and consequently, a large value of $\sigma_{\ln x}$, typically in excess of 2.5. These high values in turn imply large turbulent Mach numbers ($\mathcal{M} > 45$, corresponding to 8.6 km s^{-1} at 10 K or 30 km s^{-1} at 100 K; Padoan et al. 1997, Eqs. 4 and 5). This situation may have resulted from the passage of a powerful shock wave, e.g. one caused by a collision with an expanding bubble driven by supernova explosions and stellar winds from an OB association.

The density distribution for a slightly smaller density dispersion, $\sigma_{\ln x} = 2.2$, and the resulting mass distribution are illustrated in Figs. 11c and d, respectively. The latter Figure shows the probability density function of 'equilibrium masses', $\Phi_E(m)$, obtained from Eqs. 2 and 7, and the corresponding distribution of Jeans' masses, $\Phi_J(m)$, together with the 'mother' distribution of all clumps, assumed to follow the power law $m^{-1.5}$. The value of $\sigma_{\ln x}$ is chosen so that $\Phi_E(m)$ decreases towards higher masses, but the function still shows the characteristic peaking towards zero, which cannot be distinguished at larger values of $\sigma_{\ln x}$. The peak near zero is the contribution of low-density, pressure balanced clumps, whereas the smooth curve peaking near $3M_{\odot}$ represents dense, gravitationally bound clumps. The latter distribution resembles that of the Jeans' masses, but is flatter.

The clumps detected in this study are likely to bath in 'interclump' gas with the density just below the critical density of the C¹⁸O($J = 1 - 0$) line, i.e. about 10^3 cm^{-3} . Assuming that the external pressure 10^{-12} Pa is caused by turbulence in this interclump gas, and that the gas temperature remains at 10 K also there, we find that the required turbulent velocity dispersion is 0.5 km s^{-1} or that the rms Mach number is about 3, i.e. 15 times lower than the one consistent with the observed mass distribution according to the model of Padoan & Nordlund 2002.

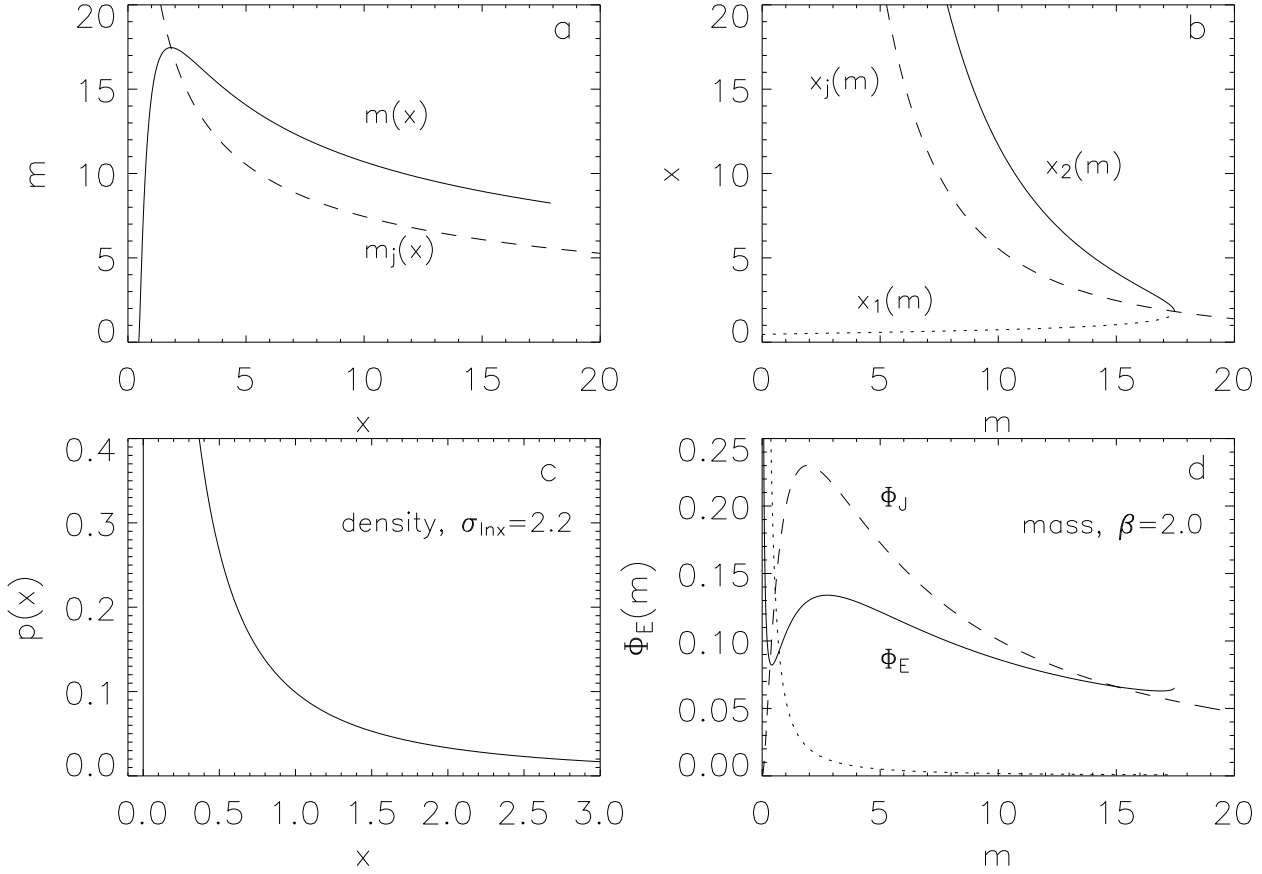


Fig. 11. a) The ‘equilibrium mass’ $m(x)$, i.e. the clump mass as a function of the density parameter $x \equiv n/\bar{n}$ (solid line). The physical parameters used here correspond to values estimated for the C¹⁸O clumps in Cha I: $P_{\text{ext}} = 110^{-12}$ Pa, $\bar{n} = 5.5 \cdot 10^3 \text{ cm}^{-3}$, $T = 10$ K, $\sigma_v = 260 \text{ ms}^{-1}$. The Jeans’ mass, m_j , for these conditions is plotted with a dashed line. **b)** Density parameter x as a function of mass, i.e. the inverse of $m(x)$ in two regions $x_1(m)$ (dotted line, low densities) and $x_2(m)$ (solid line, high densities). The corresponding function for Jeans’ masses, x_j , is plotted with the dashed line. **c)** The assumed lognormal density distribution, $p(x)$, with the standard deviation $\sigma_{\ln x} = 2.2$. **d)** The probability density function of equilibrium masses, $\Phi_E(m)$. The distribution of the Jeans’ masses, $\Phi_J(m)$, is plotted as a dashed curve. The dotted curve represents the assumed mass distribution of all dense cores (not in scale). It follows the power law $m^{-1.5}$, which is consistent with compressing turbulence.

The discrepancy may be partly explained by the hierarchical structure of turbulence. If the rms Mach number 3 is characteristic for the length scale 0.1 pc (corresponding to the typical size of a clump), $\mathcal{M} = 45$ ($\sigma_v \approx 8.5 \text{ km s}^{-1}$) should then characterize turbulence in the length scale 20 pc, assuming that the scaling law is $\sigma_v \propto L^{0.5}$ valid for compressible turbulence. This length scale corresponds to the size of the whole Chamaeleon dark cloud complex including the clouds I, II and III. The time scale, L/σ , associated with it is 3 Myr, meaning that in this time the large-scale turbulence should have decayed into motions on small scales. The ages of the star associations do not contradict with this time scale. As discussed in Sect. 3.2., a large fraction of the stars associated with the Cha I are visible pre-main-sequence stars, which indicates that at least a time on the order of 10^6 years has passed since the initiation of star formation and the possible violent event triggering it. On the other hand, if the quoted scaling law is valid, one could expect to see a larger dispersion in the radial velocities of the clumps across the cloud, i.e. over a projected distance

of about 4 pc, than the value 0.35 km s^{-1} mentioned earlier in this Section.

The exercise performed above shows that the origin of the observed clump mass distribution may be explained by the turbulent fragmentation model of Padoan & Nordlund 2002 if turbulence has initially been hypersonic, but cascaded down to much smaller scales and speeds by now. The deduced present-day velocity dispersion in the interclump gas suggest that the length scale has initially been larger than the whole Cha I cloud. According to numerical simulations turbulence acting on large scales gives rise to extensive filaments of dense gas (e.g. Klessen 2003), and the structure observed in Cha I could be readily understood. However, as discussed in Sect. 3.3 the well-ordered magnetic field is not consistent with this picture. Moreover, it is not clear from simulations if the velocity dispersion across the cloud can become as low as observed in Cha I in the turbulent fragmentation process.

In view of the fact that the region studied here may cover only a small fraction of the structure formed in this process, it is questionable how well it can reflect the global properties of the flow. We therefore do not proceed to a quantitative analysis, but intend to present such in a subsequent paper with a more varied sample of clumps, obtained by combining results from different clouds belonging to the same complex and using different clump identification algorithms.

7. Conclusions

The C¹⁸O ($J = 1 - 0$) map of the Chamaeleon I cloud with an angular resolution of $\sim 1'$ shows a network of filaments with the likeness of some recent simulations of molecular cloud fragmentation driven by large scale turbulence (e.g. Klessen 2001). These filaments seem to have, however, preferential directions, which change from N-S in the north to NE-SW in the other parts. 'Cores' identified in the previous NANTEN map (Mizuno et al. 1999) break up into a number of substructures, which we call 'clumps'. We have analyzed the small scale structure using the 'Clumpfind' routine (Williams et al. 1994) and identified about 70 separate clumps in the (x, y, v) data cube. The RMS noise level of these data limits the detectable clump spectrum to masses above $0.5M_{\odot}$. The inspection of the clump masses and kinematics shows that none of these clumps is a gravitationally bound entity, unless a large fraction of the mass is hidden from C¹⁸O observations because of depletion. However, a low external pressure of about 10^{-12} Pa ($P/k \sim 7 \cdot 10^4 \text{ cm}^{-3}\text{K}$) would be sufficient to bring some 40 clumps to a balance. This kind of pressure could be caused by turbulent interclump medium ($n \sim 10^3 \text{ cm}^{-3}$) with a velocity dispersion of $\sigma_v = 0.5 \text{ km s}^{-1}$ or a magnetic field with a strength of $16 \mu\text{G}$.

Using the analytical model for turbulent fragmentation presented in Padoan et al. 1997 and Padoan & Nordlund 2002 we derived a theoretical mass spectrum for clumps in virial equilibrium by help of external pressure. It turned out that large turbulent Mach numbers are required to produce a mass spectrum peaking at low masses as observed, and that corresponding turbulent velocity dispersion clearly exceeds the interclump velocity dispersion quoted above. A possible reason for the discrepancy is that the turbulence in the cloud has decayed since the hypothetical equilibrium clumps formed. Alternatively all condensations seen in the C¹⁸O map are just transient structures. In any case, gravitationally bound protostellar cores, such as Cha-MMS1 and Cha-MMS2 probably are, represent subcondensations of C¹⁸O 'clumps'.

Although the clump mass distribution may be understood in terms of turbulent fragmentation models, one observational result is not easily explainable by them, namely, the well-ordered magnetic field structure in the cloud. The magnetic field direction as determined from the polarization position angles of highly reddened background stars is perpendicular to the general orientation of dense filaments, suggesting a magnetically controlled collapse (McGregor et al. 1994).

We consider it possible that different processes are taking effect on different scales. Although large scale magnetic fields are likely to have influenced the formation of the filaments,

their fragmentation into smaller clumps may have been dominated by chaotic motions. In the sequel, we intend to perform direct comparisons between the observational data (spectra and column density distributions) and simulation results in order to determine the characteristics of the turbulence and thereby gain better understanding of its rôle in the cloud fragmentation.

Acknowledgements. We thank Jonathan Williams for making the IDL version of the Clumpfind program publicly available. This project was supported by the Academy of Finland, grant Nos. 73727, 74854.

References

- Ballesteros-Paredes, J. & Mac Low, M.-M. 2002, ApJ, 570, 734
 Boulanger, F., Falgarone, E., Puget, J. L. & Helou, G. 1990, ApJ, 364, 136
 Boulanger, F., Bronfman, L., Dame, T. M. & Thaddeus, P. 1998, A&A, 332, 273
 Cambr esy, L., Epchtein, N., Copet, E., de Batz, B., Kimeswenger, S., Le Bertre, T., Rouan, D. & Tiph ene, D., 1997, A&A324, L5
 Cambr esy, L., Copet, E., Epchtein, N., de Batz, B., Borsenberger, J., Fouque, P., Kimeswenger, S., & Tiph ene, D., 1997, A&A338, 997
 Carpenter, J. M., Hillenbrand, L. A., Skrutskie, M. F., & Meyer, M. R. 2002, AJ, 124, 1001
 Caselli, P., Walmsley, C. M., Tafalla, M., Dore, L., & Myers, P. C. 1999, ApJ, 523, L165
 Cederblad, S. 1946, Meddelanden fr an Lunds Astronomiska Observatorium, Serie II, 119, 1
 Frerking, M. A., Langer, W. D., & Wilson, R. W. 1982, ApJ, 262, 590
 Gahm, G. F., Lehtinen, K., Carlqvist, P., Harju, J., Juvela, M. & Mattila, K. 2002, A&A, 389, 577
 G omez, M. & Kenyon, S. J. 2001, AJ121, 974
 Goodman, A. A., Jones, T. J., Lada, E. A., & Myers, P. C. 1992, ApJ, 399, 108
 Haikala, L. K., Mattila, K., Lehtinen, K. & Lemke, D. 1998, ASP Conf. Ser. 132: Star Formation with the Infrared Space Observatory, 147
 Harjunp aa, P. & Mattila, K. 1996, A&A, 305, 920
 Hayakawa, T., Mizuno, A., Onishi, T., Hara, A., Yamaguchi, R. & Fukui, Y. 1999, PASJ, 51, 919
 Jones, T. J., Hyland, A. R., Harvey, P. M., Wilking, B. A. & Joy, M. 1985, AJ, 90, 1191
 Kenyon, S. J. & G omez, M. 2001, AJ, 121, 2673
 Klessen R.S. 2001, ApJ, 556, 837
 Klessen R.S. 2003, in Reviews in Modern Astronomy, Vol. 16, astro-ph/0301381
 Knude, J. & H og, E. 1998, A&A, 338, 897
 Larson, R. B. 1979, MNRAS, 186, 479
 Larson, R. B. 1981, MNRAS, 194, 809
 Lehtinen, K., Haikala, L. K., Mattila, K. & Lemke, D. 2001, A&A, 367, 311
 Lehtinen, K., Harju, J., Kontinen, S. & Higdon, J.L. 2003, A&A, 401, 1017
 Mattila, K., Liljestr om, T. & Toriseva, M. 1989, Proc. ESO Workshop on Low Mass Star Formation and Pre-main Sequence Objects, 153
 McGregor, P. J., Harrison, T. E., Hough, J. H., & Bailey, J. A. 1994, MNRAS, 267, 755
 Mizuno, A., Hayakawa, T., Yamaguchi, N., et al. 1998, ApJ, 507, 83
 Mizuno, A., Hayakawa, T., Tachihara, K., et al. 1999, PASJ, 51, 859
 Mizuno, A., Yamaguchi, R., Tachihara, K., et al. 2001, PASJ, 53, 1071
 Myers, P. C., Ladd, E. F., & Fuller, G. A. 1991, ApJ, 372, L95
 Padoan, P. & Nordlund,  . 2002, ApJ, 576, 870
 Padoan, P., Nordlund,  . & Jones, B.J.T. 1997, MNRAS, 288, 145

- Persi, P., Marenzi, A. R., Kaas, A. A., Olofsson, G., Nordh, L., & Roth, M. 1999, *AJ*, 117, 439
- Persi, P., Marenzi, A.R. & Olofsson, G. 2000, *A&A*, 357, 219
- Persi P., Marenzi A.R., Gómez M. & Olofsson G. 2001, *A&A*, 376, 907
- Prusti, T., Clark, F.O., Whittet, D.C.B., Laureijs, R.J. & Zhang, C.Y. 1991, *MNRAS*251, 303
- Schwartz, R. D. 1991, *Low Mass Star Formation in Southern Clouds*, ESO Scientific Report No.11, 1991, ed. B. Reipurth, p. 93
- Reipurth, B., Nyman, L.-Å. & Chini, R. 1996, *A&A*, 314, 258
- Tachihara, K., Onishi, T., Mizuno, A. & Fukui, Y. 2002, *A&A*, 385, 909
- Toriseva, M. & Mattila, K. 1985, *A&A*, 153, 207
- Toriseva, M., Höglund B. & Mattila, K. 1985, *Rev. Mexicana Astron. Astrof.*, 10 135
- Toriseva, M., Mattila, K., & Bronfman, L. 1990, *Ap&SS*, 171, 219
- Tóth, L. V., Hotzel, S., Krause, O., Lehtinen, K., Lemke, D., Mattila, K., Stickel, M. & Laureijs, R. J. 2000, *A&A*, 364, 769
- Whittet, D. C. B., Gerakines, P. A., Carkner, et al. 1994, *MNRAS*, 268, 1
- Williams, J. P., de Geus, E. J. & Blitz, L. 1994, *ApJ*, 428, 693
- Wilson, T. L. & Rood, R. 1994, *ARA&A*, 32, 191

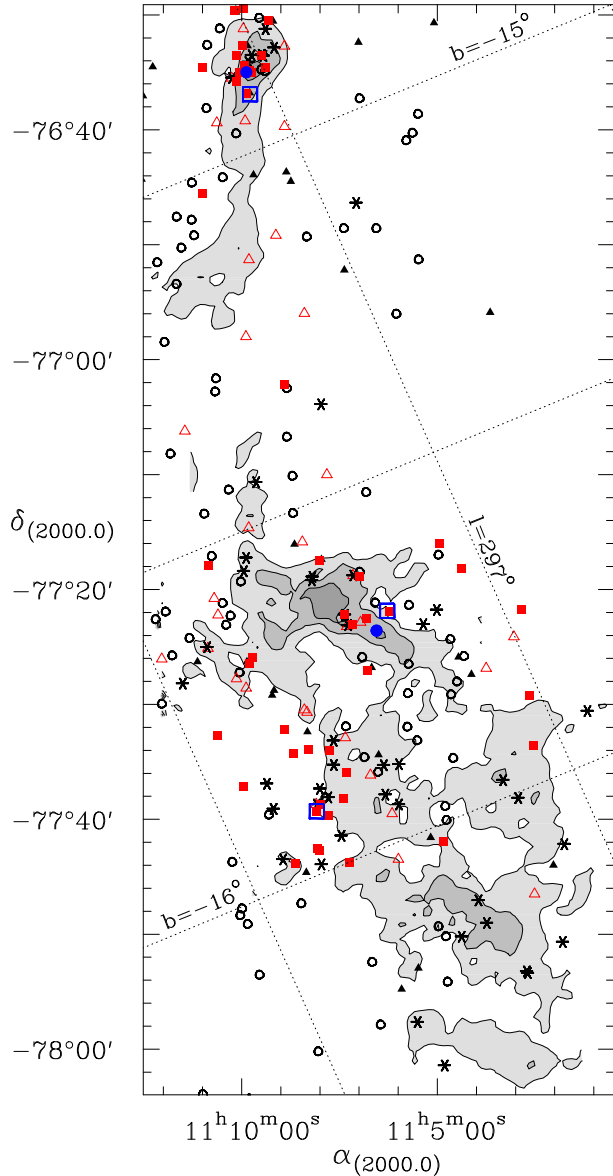


Fig. 7. Cha I association members and candidate members projected on the integrated C¹⁸O intensity map of the cloud. Sources of the coordinates are Schwartz 1991 (Optical candidate members, black triangles), Persi et al. 2000 (known members with NIR excess, red squares, member candidates with NIR excess, open red triangles), Cambrésy et al. 1998 (new Young Stellar Object candidates, asterisks) and Gómez & Kenyon 2001 (candidate pre-main-sequence stars, open circles). The locations of the reflection nebulae Ced 112, Ced 110 and Ced 111 (from north to south) are indicated with open squares. The locations of the Class 0 protostar candidates Cha-MMS1 and Cha-MMS2 are indicated with filled circles.

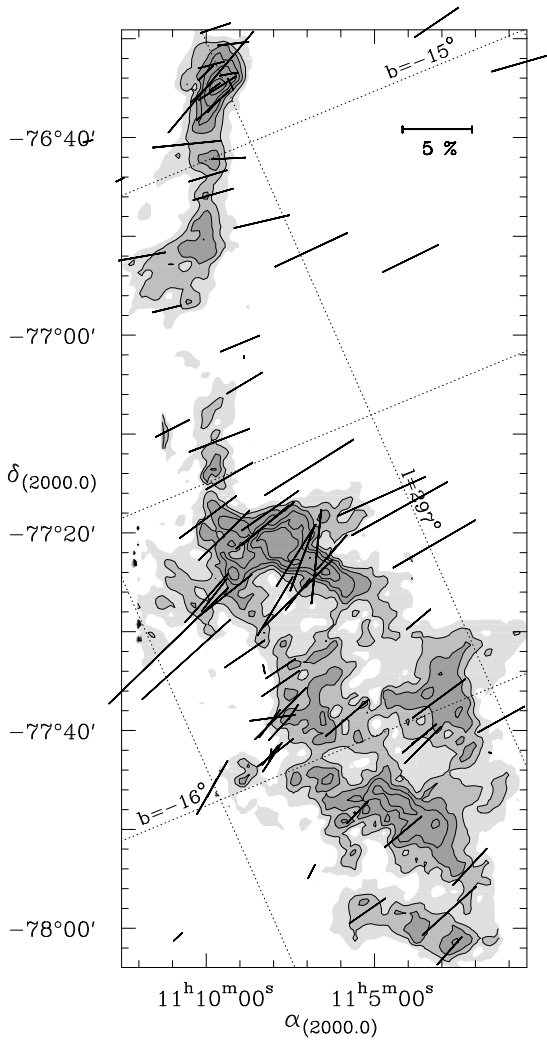


Fig. 8. Polarization vectors of field stars and Cha I members (Whittet et al. 1994, McGregor et al. 1994) superposed on the integrated C¹⁸O intensity map of Cha I.

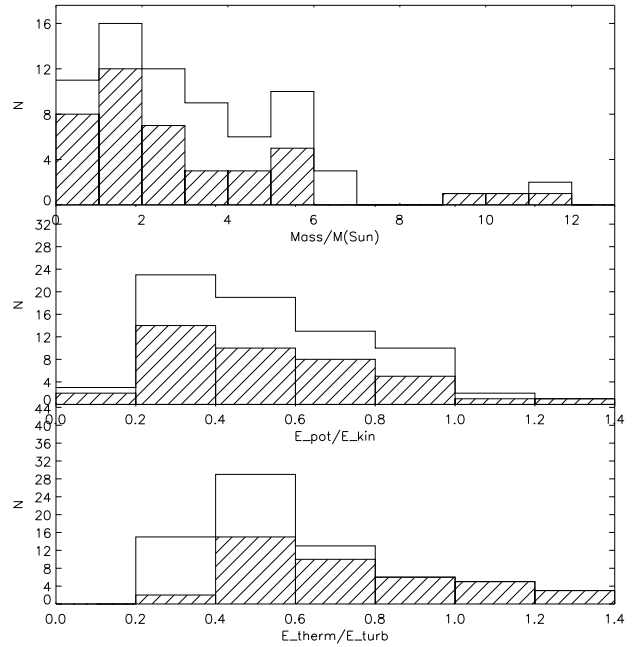


Fig. 9. **Top:** Distribution of the clump masses in Cha I. **Middle:** The ratios of the gravitational potential to the kinetic energies, $|E_{\text{pot}}|/E_{\text{kin}}$. The kinetic energy estimates contain both the internal thermal energy and the energy of the turbulent motions. **Bottom:** The ratios of thermal to turbulent energies. The hatched columns correspond to clumps which possibly are in virial equilibrium (see text).

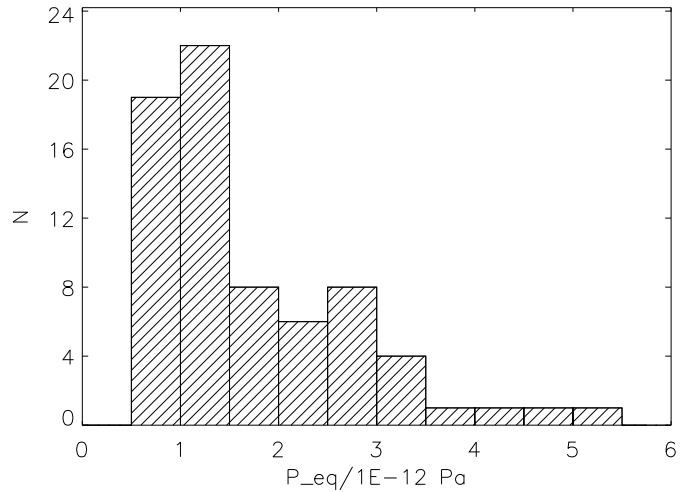


Fig. 10. The distribution of external pressures, P_{ext} needed to stabilize the identified clumps.